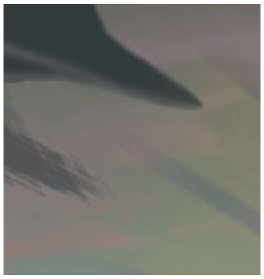

Imaging a BQM-74E Target Drone Using Coherent Radar Cross Section Measurements

Allen J. Bric

Since the early 1980s and the advent of the modern computer, digital radar imaging has developed into a mature field. In this article, the specific problem of imaging a rotating target with a stationary radar is reviewed and built upon. The relative motion between the rotating target and the stationary radar can be used to create a circular synthetic aperture for imaging the target. Typically, an image is reconstructed by first reformatting the raw data onto a two-dimensional grid in the spatial frequency domain (commonly referred to as *k*-space) and then inverting into the spatial domain using a Fourier transform. This article focuses on a less popular reconstruction paradigm, tomographic processing, which can be used to coherently reconstruct the image incrementally as data become available. Both techniques suffer from sidelobe artifacts. It is shown that one-dimensional adaptive windowing can be applied during the reconstruction phase to reduce sidelobe energy while preserving mainlobe resolution in the image plane. The algorithms are applied to real and simulated radar cross section data.

(Keywords: BQM-74E, Radar imaging, Spatially variant apodization, SVA, Synthetic aperture radar, Tomography.)

INTRODUCTION

Until 1979, synthetic aperture radar (SAR) images were formed using analog techniques, incorporating optical lenses and photographic film. In 1979, the first reconstruction of a SAR image was formed on a digital computer.[1] Today, provided the data are available, SAR images can be formed on relatively inexpensive personal computers, which have replaced expensive optical processors and mainframe computers. This ability has led to an explosion of SAR processing techniques over the past decade. Radar imaging is now an invaluable instrument in many scientific fields.

A radar image is formed by illuminating a scene and resolving the resulting scattering distribution into range and cross-range dimensions, where the range component measures a reflector's radial distance from the radar. This procedure provides a two-dimensional map of the spatial scattering distribution. Two components are essential for providing this spatial resolution: frequency diversity and spatial diversity.

Frequency diversity provides range resolving capabilities and is achieved by using a wideband radar to illuminate the target scene. After the wideband return data are processed, a range profile, or projection, can be generated that characterizes the scattering distribution of the scene along the range axis. This profile is a one-dimensional projection of the three-dimensional spatial scattering distribution onto the range axis. The profile is resolved into range cells whose resolution is inversely proportional to the bandwidth of the transmit signal. The energy returned from each cell is the integrated contribution of all scatterers inside the antenna beam in that particular range cell. Since the beamwidth of a reasonably sized real antenna at radio frequencies generates a correspondingly large cross-range cell in the far field, the fine resolution necessary to resolve small targets in the cross-range (azimuth) direction cannot be obtained directly.

To further resolve the target scene into the cross-range dimension, the radar system must have either a large aperture or spatial diversity. This requirement can be met by using a real array of antennas; at radio frequencies, however, a large and expensive array is necessary to generate reasonable resolution (i.e., 0.1–2.0 m). To solve this problem, the relative motion between the target scene and the radar can be used to generate the necessary spatial aperture. This is the basis of SAR, which was discovered by Carl Wiley in 1951.[1,2] This article concerns only SAR processing where the relative motion between the target and the radar forms a circular antenna aperture. If the target is held stationary while the radar platform traces out the circular aperture, the processing is called spotlight-mode SAR (Fig. 1a). An equivalent result can be obtained if the radar can be held stationary while the target is rotated to provide the relative motion (Fig 1b). Whenever the object's motion is used to generate the synthetic aperture, the processing is called inverse SAR (ISAR). For the rest of this article, ISAR processing refers to the specific case of a rotating object.

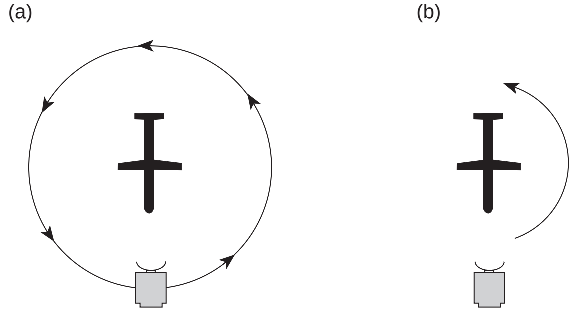

Figure 1. Illustration of relative motion where (a) the radar provides the motion, and (b) the target provides the motion for generating a circular aperture.

This article reviews the tomographic process and its application to SAR imaging when the relative motion between the object and the radar generates a circular aperture. One-dimensional adaptive sidelobe cancellation techniques are introduced into the tomographic reconstruction process. Applying adaptive processing can greatly reduce the sidelobe artifacts formed in the tomographic image without degrading spatial resolution. The results are applied to a simulated data set and to actual radar cross section (RCS) measurements performed on a BQM-74E target drone.[3]

RADAR CROSS SECTION MEASUREMENTS

RCS measurements were collected at the Naval Air Warfare Center Weapons Division's Radar Reflectivity Laboratory (RRL) in Point Mugu, California, to characterize the scattering mechanisms on the BQM-74E target drone for the Mountain Top Project. Four frequency bands (UHF, C, X, and Ka) were used. Although both bistatic and monostatic measurements were made, only the monostatic measurements are considered here. All of the monostatic RCS measurements made on the BQM-74E were collected in RRL's large anechoic chamber, which has a usable range length of 72 ft. To provide far-field measurements, a Scientific-Atlanta compact range collimating reflector with a 16-ft quiet zone was used as a plane-wave transducer. During the data collection, the drone was rotated through 180° in 0.1° angular increments. At each step, it was illuminated with a swept linear-FM radar, and the return was sampled and recorded on an HP 9000 computer.[3] Frequency sampling at X and C band provided 15 m of unambiguous range extent.

The BQM-74E (Fig. 2a) is a reusable subsonic turbojet-powered target drone used primarily to simulate a low-altitude antiship missile. It has a fuselage length of 12.9 ft, a wing span of 5.8 ft, and a maximum fuselage diameter of 14 in. Since these drones are used for a variety of missions, optional payload kits can be installed to change their functional configurations. For the Mountain Top experiment, the drones were modified to an LEC-305 configuration, which consists of seven different antennas and a metal-taped, fiberglass nose cone that reduces RCS by shielding internal components.[3] The antenna placements are shown in Fig. 2b.

TOMOGRAPHIC PROCESSING

This section reviews the basic concepts necessary for understanding the tomographic process and shows how these concepts are applied to reflection tomography or,

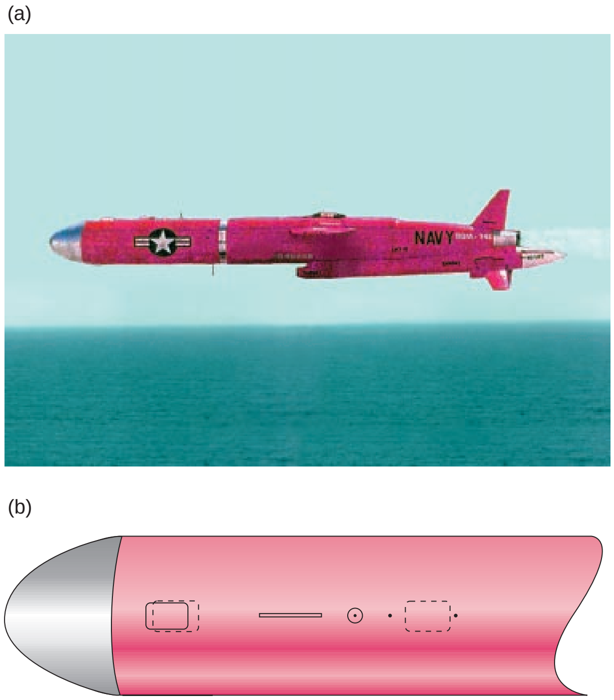

Figure 2. BQM-74E target drone (a) in flight, and (b) with antenna placements used in the tests for the Mountain Top Project. Dashed lines indicate the position of antennas on the underside of the fuselage.

more specifically, to radar imaging.[4,5] Tomography attempts to reconstruct an object (form an image) from its one-dimensional projections. In X-ray tomography, the projections are density measurements, whereas in radar tomography, they are range profiles (see the boxed insert, Range Processing). We start by examining the simple case of inverting, or "imaging," an object with rotational symmetry and then showing how the Fourier slice theorem is used to extend this process to non–rotationally symmetric objects. Next a simple nondiffracting, parallel ray, coherent back-projection algorithm is considered for reconstructing the images. In all the following calculations, it is assumed that the target is illuminated in the antenna's far field.

Rotational Symmetry

Two-dimensional rotationally symmetric functions can be "imaged" by considering the Fourier–Abel–Hankel cycle (see the boxed insert for a review of this cycle). Tomographic imaging is a natural extension of this cycle for non–rotationally symmetric functions. The immediate implication of this cycle is that the Hankel and Abel transforms can be calculated without having to compute Bessel functions and derivatives, respectively. Another implication is that a two-dimensional rotationally symmetric function can be inverted by computing the Abel transform (finding its projection), and following with a one-dimensional Fourier transform, instead of requiring a two-dimensional Fourier transform. This result is pleasing but is not practical in real imaging situations, because the object to be imaged is rarely circularly symmetric. The result can be extended to nonsymmetric functions, however, through the use of the Fourier slice theorem.

RANGE PROCESSING

Before examining any imaging techniques, it is useful to review the process of generating a range profile. Range processing is a basic concept that can be explained in terms of propagation delay and Fourier analysis. A radar can measure the range to a target by determining the propagation delay. If the radar is monostatic, the range R is simply

$$R = \frac{c\tau}{2} , \tag{A}$$

where τ is the propagation delay, and c is the speed of light. If the transmitted signal has a finite bandwidth, the range resolution can be determined by considering a unit time–bandwidth product. The range resolution equation becomes

$$\Delta R = \frac{c}{2B} , \tag{B}$$

where B is the transmitted bandwidth. It follows that the range resolution is inversely proportional to the transmitted bandwidth.

Generating a range profile requires that the scattering mechanisms be properly sorted into range cells dictated by the transmitted bandwidth. If the transmitted signal is modeled as a sum of complex sinusoids subtending the bandwidth, the total return from one transmitted pulse will be

$$G(f) = \int_{-\infty}^{\infty} s(t) e^{j2\pi f t}\, dt , \tag{C}$$

where $s(t)$ is the scattering distribution represented as a function of time t (range). It is clear from Eq. C that the radar return measures the Fourier transform of the scattering distribution over the defined bandpass region. An estimate of the scattering distribution may now be obtained by inverting the Fourier transform:

$$\hat{s}(t) = \int_{f_0-B/2}^{f_0+B/2} G(f) e^{j2\pi f t}\, df + \int_{-f_0-B/2}^{-f_0+B/2} G(f) e^{-j2\pi f t}\, df , \tag{D}$$

where $\hat{s}(t)$ is commonly referred to as the range profile and is the estimate of the scattering distribution along the range axis over a finite bandwidth. Note that Eqs. A–D assume that a large instantaneous bandwidth is transmitted. It is easily shown that these equations also hold for a synthesized bandwidth (e.g., a swept linear-FM system).[6]

THE FOURIER–ABEL–HANKEL CYCLE

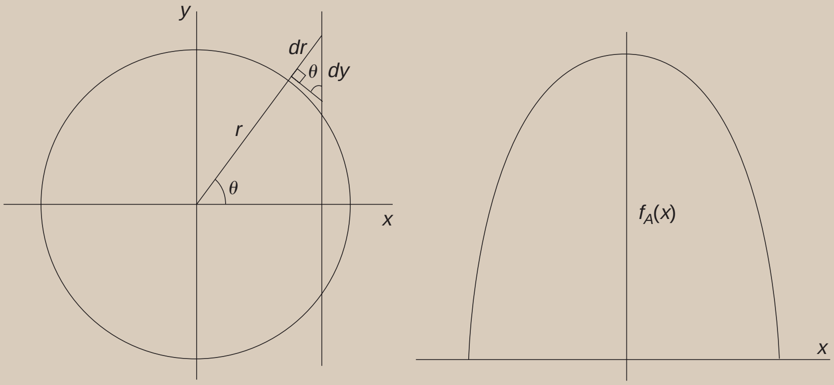

Figure A. Geometry for the Abel transform.

The zero-order Hankel transform is a one-dimensional transform that can be used to determine the two-dimensional Fourier transform of a rotationally symmetric function. This apparent simplification results from the fact that a two-dimensional rotationally symmetric function $f(x, y)$, when expressed in polar form, is dependent on only a single parameter, namely, the radial distance r, where $r=\sqrt{x^2+y^2}$, and is independent of the spatial azimuth angle θ. Furthermore, the Fourier transform $F(u, v)$ also exhibits rotational symmetry and is dependent only on the radial frequency q, where $q=\sqrt{u^2+v^2}$, and is independent of the frequency azimuth angle ϕ. A straightforward derivation of the Hankel transform is given by Bracewell[7] and is summarized as follows:

$$F(u,v)=\iint_c f(x,y)e^{-j2\pi(ux+vy)}\,dx\,dy\,, \tag{I}$$

$$F(u,v)=F(q)=\int_0^\infty\int_0^{2\pi} f(r)e^{-j2\pi qr\cos(\theta-\phi)}r\,dr\,d\theta\,, \tag{II}$$

where $f(r)$ and $F(q)$ are the polar representations of the rotationally symmetric functions $f(x, y)$ and $F(u, v)$, respectively, and c is the speed of light. After some manipulation, Eq. II can be expressed as

$$F(q)=2\pi\int_0^\infty f(r)J_0(2\pi qr)r\,dr\,, \tag{III}$$

where $F(q)$ is defined as the zero-order Hankel transform of $f(r)$, and J_0 is the zero-order Bessel function.

The Abel transform is used to describe the one-dimensional “density” projection or line integral of a two-dimensional function. For rotationally symmetric functions, this line integral is identical in all directions; thus, it can be defined on any axis.[7] For convenience, it is defined on the x axis as

$$f_A(x)=\int_{-\infty}^{\infty} f\left(\sqrt{x^2+y^2}\right)dy\,. \tag{IV}$$

Using Fig. A, and noting that $dr/dy = \sin\theta=\sqrt{r^2-x^2}\big/r$, an alternative definition expressed in terms of r is given by

$$f_A(x)=2\int_x^\infty \frac{f(r)r}{\sqrt{r^2-x^2}}\,dr\,. \tag{V}$$

The inverse Abel transform, derived by Bracewell,[8] is presented here as

$$f(r)=-\frac{1}{\pi}\int_r^\infty \frac{f'_A(x)}{\sqrt{x^2-r^2}}\,dx\,. \tag{VI}$$

Inverting the Abel transform numerically using Eq. VI requires determining a derivative. Since numerical errors can occur during this operation and are exacerbated by the integration, a better method is to use the Fourier–Abel–Hankel cycle for inversion. This cycle is valid for circular symmetric functions whose cross section is by definition an even function. Given that the Fourier transform of an even function is its own inverse (i.e. $F = F^{-1}$), Bracewell[7] proved that

$$\begin{array}{lll} HFA = I & AHF = I & FAH = I \\ FHA^{-1} = I & HA^{-1}F = I & A^{-1}FH = I\,, \end{array} \tag{VII}$$

where I is the identity transform, H is the zero-order Hankel transform, and A is the Abel transform. Using the identities $HH = I$ and $FF = I$ with the preceding identities, the following equations are easily derived:

$$\begin{array}{lll} H = FA & A = FH & F = AH \\ H = A^{-1}F & A^{-1} = HF & F = HA^{-1}\,. \end{array} \tag{VIII}$$

These equations form the basis of the Fourier–Abel–Hankel cycle shown in Fig B.

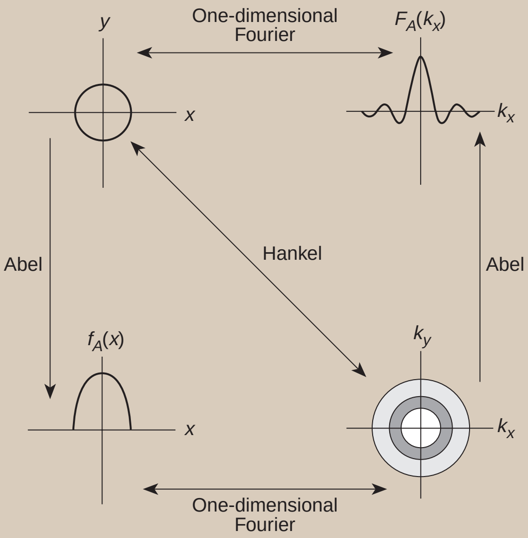

Figure B. Fourier–Abel–Hankel cycle (based on Bracewell,[7] Fig. 14-4).

Fourier Slice Theorem

The Fourier slice theorem removes the rotational symmetry requirement from the Fourier–Abel–Hankel cycle (and effectively removes the Hankel transform, since it is valid only for two-dimensional rotationally symmetric functions). The modified cycle is given in Fig. 3.

The Fourier slice theorem simply states that the Fourier transform of an object's projection (Abel transform) will yield a slice of the two-dimensional Fourier transform oriented at the same angle as the projection. For completeness, this result is derived as follows:

Consider the rotated coordinate frame of Fig. 4, where $x' = x\cos\theta + y\sin\theta$ and $y' = y\cos\theta - x\sin\theta$ define the projection onto the x' axis as

$$p_\theta(x') = \int_{-\infty}^{\infty} s(x', y')\,dy' . \tag{1}$$

Taking the Fourier transform of the projection, we have

$$\begin{aligned} P_\theta(f) &= \int_{-\infty}^{\infty} p_\theta(x') e^{-j2\pi f x'}\,dx' , \\ &= \int_{-\infty}^{\infty}\int_{-\infty}^{\infty} s(x',y') e^{-j2\pi f x'}\,dx'\,dy' \\ &= \int_{-\infty}^{\infty}\int_{-\infty}^{\infty} s(x,y) e^{-j2\pi f(x\cos\theta + y\sin\theta)}\,dx\,dy , \end{aligned} \tag{2}$$

where f is frequency. Relating Eq. 2 to the two-dimensional Fourier transform, we have

$$P_\theta(f) = S(f,\theta) = S(f\cos\theta, f\sin\theta) . \tag{3}$$

Thus, it has been shown that the Fourier transform of an object's projection is equivalent to a slice of its two-dimensional Fourier transform oriented at the projection angle.

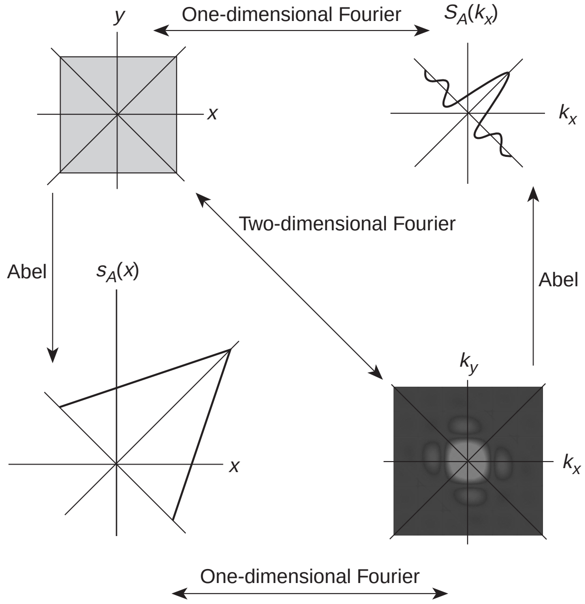

Figure 3. Cycle of transforms implied by the Fourier slice theorem (based on Bracewell,[7] Fig. 14-5).

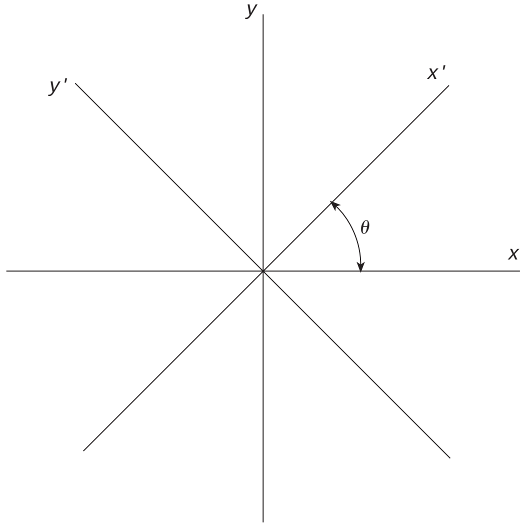

Figure 4. Geometry for derivation of the Fourier slice theorem (θ = azimuth angle).

The Fourier slice theorem provides another means for calculating the Fourier transform of a two-dimensional scene. Unfortunately, it provides no computational advantage. If the projections are provided, however, then the two-dimensional Fourier transform can be built rapidly. Typically, this direct method is not used because the Fourier transform of the projection is not available, but in radar systems, the projection's Fourier transform is measured directly. Therefore, this method is computationally efficient in forming the two-dimensional Fourier transform of the scene. This is nice, but the real interest lies in imaging the object scene, not its Fourier transform. The problem of imaging the scene now involves applying a two-dimensional inverse Fourier transform. For an equivalent result, one could project the two-dimensional Fourier transform at various angles and then take an inverse Fourier transform of each resulting projection to recover a slice of the object scene along the angle of projection; however, this method is ill-advised because it is so computationally inefficient.

Both of the aforementioned methods for inverting the two-dimensional Fourier transform require that the entire frequency domain description be available. Since projections are collected serially, it would be beneficial if one could perform the image reconstruction by combining the projections directly to get the final image; thus, the image could be formed iteratively. This method of image reconstruction is called back-projection.

Back-Projection

Back-projection was devised as a technique to reconstruct straight-ray tomographic images. The basic idea is to shadow each projection (properly oriented) over the image scene and sum the shadows to form an image. This algorithm is easily derived by rewriting the Fourier slice theorem.[5]

The inverse two-dimensional Fourier transform in rectangular coordinates is given by

$$s(x,y) = \int_{-\infty}^{\infty} \int_{-\infty}^{\infty} S(u,v) e^{j2\pi(ux+vy)} \, du \, dv \, . \tag{4}$$

Changing to polar coordinates with $u = f \cos \theta$ and $v = f \sin \theta$, the transform can be rewritten as

$$s(x,y) = \int_{0}^{2\pi} \int_{0}^{\infty} S(f,\theta) e^{j2\pi f(x\cos\theta + y\sin\theta)} f \, df \, d\theta \, . \tag{5}$$

Expanding the preceding integral into two integrals from 0 to π and π to 2π gives

$$\begin{aligned} s(x,y) = & \int_{0}^{\pi} \int_{0}^{\infty} S(f,\theta) e^{j2\pi f(x\cos\theta + y\sin\theta)} f \, df \, d\theta \\ & + \int_{0}^{\pi} \int_{0}^{\infty} S(f,\theta+\pi) e^{j2\pi f[x\cos(\theta+\pi) + y\sin(\theta+\pi)]} f \, df \, d\theta \, . \end{aligned} \tag{6}$$

Recall that $\cos(\theta + \pi) = -\cos \theta$ and $\sin(\theta + \pi) = -\sin \theta$ and $S(-f, \theta) = S(f, \theta + 180)$. After substituting and simplifying, we have

$$s(x,y) = \int_{0}^{\pi} \int_{-\infty}^{\infty} S(f,\theta) e^{j2\pi f(x\cos\theta + y\sin\theta)} |f| \, df \, d\theta \, . \tag{7}$$

Substituting Eq. 3 in Eq. 7 and changing coordinates with respect to Fig. 4 yield

$$s(x,y) = \int_{0}^{\pi} \int_{-\infty}^{\infty} P_\theta(f) e^{j2\pi f x'} |f| \, df \, d\theta \, . \tag{8}$$

Note that the inner integral in Eq. 8 is just the projection $p_\theta(x')$ filtered by a factor $|f|$. Define the filtered projection as

$$q_\theta(x') = \int_{-\infty}^{\infty} P_\theta(f) |f| e^{j2\pi f x'} \, df \, . \tag{9}$$

Now, substituting Eq. 9 in Eq. 8 gives the back-projection equation:

$$\begin{aligned} s(x,y) &= \int_{0}^{\pi} q_\theta(x') \, d\theta \, , \\ s(x,y) &= \int_{0}^{\pi} q_\theta(x\cos\theta + y\sin\theta) \, d\theta \, . \end{aligned} \tag{10}$$

From Eqs. 9 and 10 it is clear that the image is constructed successively as each projection is acquired. This process enables the image to be constructed serially, eliminating the need to wait for all projections to become available for processing to begin. At each step, the resulting image can be viewed, with successive projections increasing its fidelity. In some circumstances the intermediate images may provide valuable information (e.g., target identification or classification processors).

At a first glance, the high-pass filtering operation implied by Eq. 9 may not seem unusual, but a closer inspection reveals that the square of the filter function $|f|$ is not integrable, which implies that its Fourier transform does not exist. This integral can be approximated, as is shown by Kak[4] and Bracewell.[7] If one numerically performs the integration implied by Eq. 9, the resulting image will have lost its DC component and will be distorted because of periodic convolution and interperiod interference.[4] An exact solution for the integral exists if the filter can be band-limited. This condition can be asserted without loss of generality because the projection is a real signal and is therefore band-limited. For the band-limited case, the impulse response of the filter becomes

$$\begin{aligned} h(x') &= \int_{-B/2}^{B/2} |f| e^{j2\pi f x'} \, df \, , \\ h(x') &= \frac{1}{2\tau^2} \frac{\sin(2\pi x'/2\tau)}{2\pi x'/2\tau} - \frac{1}{4\tau^2} \left[\frac{\sin(\pi\tau/2\tau)}{\pi\tau/2\tau} \right]^2 , \end{aligned} \tag{11}$$

where B is the transmitted bandwidth and $\tau = 1/B$. In the preceding case, the impulse response is computed only over a finite interval and is then inverted, causing its response to depart from the ideal response at lower frequencies. Since only a finite number of points in the impulse response are considered, the frequency response tails off to a positive number slightly above zero at DC.[4] This offset maintains the actual DC level of the image and also removes the distortion caused by the interperiod interference. When this correction is applied to the projections, the reconstruction process is called filtered back-projection. It is important to point out that this correction is unnecessary in the tomographic computation of circular aperture radar images, because the Fourier data typically exist only along an annular region in the spatial frequency domain (k-space) and therefore naturally act as a "high-pass" filter, similar to Eq. 11.[6,9,10]

Reflective Tomography

The equations derived in the previous section describe a method used in straight-beam X-ray tomography where diffraction effects do not occur. (Other derivations exist, such as fan-beam tomography.) Since a density projection is measured by an X-ray, it is assumed that a rotation of 180° will produce an identical (but rotated) density projection. Note that this is not the case when electromagnetic waves are used, as diffraction and refraction effects can occur when an object is illuminated. In this case, to completely characterize the object, a 360° rotation is required. It can be shown, however, that these straight-beam equations are a good approximation for reflective tomography if the object is in the far field of the radiating source or, equivalently, if a plane-wave transducer is used.[4] In this article, we use the straight-beam equations as derived in the previous section (without the filtering), along with a target rotation of 180°, to reconstruct the images (data were unavailable for a target rotation of 360°).

Sidelobe Reduction

One problem prevalent in both conventional SAR and tomographic SAR imagery is range sidelobes. Wherever the target has a sizable RCS, energy can "bleed" into other range and cross-range cells, forming sidelobes. Sidelobes can greatly degrade image quality and mask details in the computed image. Since the back-projection technique synthesizes an image concurrently as projections become available, it is desirable to window the projections directly, reducing their sidelobes, prior to back-projecting. Clearly, reducing the sidelobes in the range profile (projection) will reduce the sidelobes in the resulting image. This section focuses on one-dimensional windowing techniques for reducing sidelobes in the range profile.

Hanning Window

A simple but effective technique for reducing sidelobes is to window the data with a raised cosine window. This window can be applied to the spatial frequency data prior to zero padding and inversion. The resulting range profile has greatly reduced sidelobes; the cost, however, is a reduction in spatial resolution. In some cases, it is unclear whether the reduced sidelobes are worth the trade-off of lower spatial resolution. When a tomographic radar image is formed with Hanning-windowed range profiles, the resulting image shows a noticeable loss of resolution.

Spatially Variant Apodization

Spatially variant apodization (SVA) is a nonlinear windowing technique that adaptively calculates the optimal type of raised cosine window at every point in the inverse domain. Apodization, a term borrowed from optics, refers to the reduction of sidelobe artifacts. This technique, devised by Stankwitz et al.,[10] provides considerable sidelobe reduction over traditional windowing while maintaining maximum resolution. The basics of this technique are easily understood by considering the effect of multi-apodization.

Multi-apodization combines the results of multiple, uniquely windowed transforms on a data segment (including a rectangular window). After the transforms are calculated, a "composite" result is formed choosing the minimum magnitude on a point-by-point basis over all of the transformed data sets. Since the transform of the rectangular window provides the narrowest mainlobe, the resulting mainlobe for the composite is identical to that of the rectangular window. Thus, the high-resolution properties of the rectangular window are preserved while the sidelobes are reduced as dictated by the properties of the windows chosen in the scheme. This technique is illustrated in Fig. 5.[10]

Multi-apodization, while simple to implement, can reduce sidelobes only to an extent dictated by the windows in the scheme. Although adding windows to this scheme can further reduce sidelobes, the computational burden of doing so ultimately limits the amount of sidelobe reduction possible. If the window type is restricted to the family of raised cosine windows, then SVA can be used to provide an effective continuum of multi-apodizations based on a raised cosine of a specific order $K - 1$. Consider the general form for the family of raised cosine windows given by

$$w_K(t) = \frac{1}{T} \sum_{k=0}^{K} \alpha_k (-1)^k \cos\left(\frac{2\pi k t}{T}\right), \qquad (12)$$

where T is the time extent of the window, $0 \leq t \leq T$ (Nuttall[11]), and α is a weighting factor. From Eq. 12,

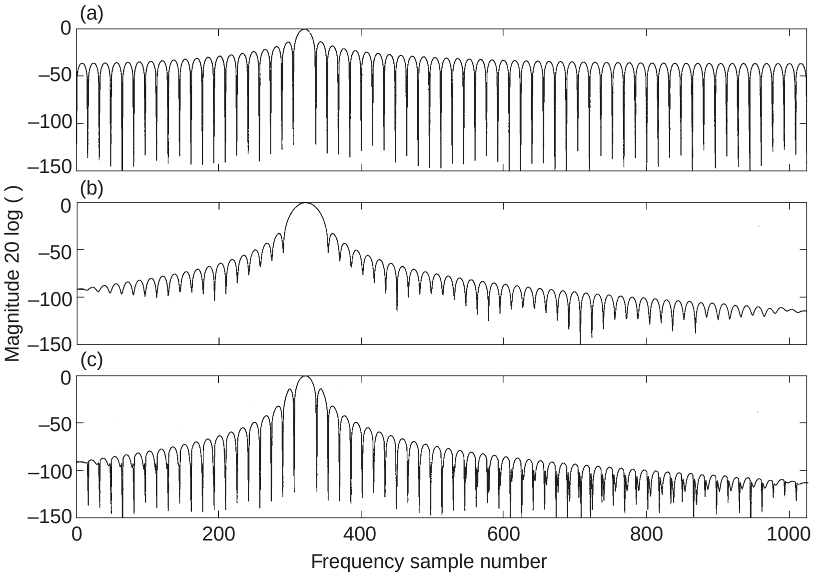

Figure 5. Results of Fourier transform on sinusoid with (a) rectangular window, (b) Hanning window, and (c) dual apodization using rectangular and Hanning windows.

it is easily seen that a $(K-1)$th-order raised cosine window will contain a constant term and $K-1$ cosine terms. For a first-order raised cosine window, only the first two terms in Eq. 12 are considered, and after normalization we have

$$w(n)=1-2\alpha\cos(2\pi n/N)\,, \qquad (13)$$

where $0 \le n \le N$. If the minimum value of Eq. 13 is constrained to be greater than zero, α is bound between zero and one-half. As α is continuously varied, an entire family of first-order raised cosine windows can be generated. With this restricted family of raised cosine windows, the SVA algorithm is tasked with determining the optimal α (window) for each point in the transformed domain. This is now equivalent to a continuum of multi-apodizations (for the family of first-order raised cosine windows), resulting in an adaptive window that optimally reduces sidelobes while maximizing mainlobe resolution. To determine α, we minimize the square magnitude in the inverse domain of the windowed data. Stankwitz et al.[10] give the derivation of the optimal α for a first-order raised cosine window, and the result is given as

$$\alpha=\mathrm{Re}\left\{\frac{g(m)}{[g(m-1)+g(m+1)]}\right\}, \qquad (14)$$

where $0 \le \alpha \le 0.5$ and $g(*)$ is the transformed data. The output can now be defined in terms of a three-point convolution between the transform of Eq. 13 and $g(*)$:

$$f(m) = g(m) + \alpha[g(m-1) + g(m+1)]\,. \qquad (15)$$

Stankwitz et al.[10] explored numerous apodization techniques, including complex dual apodization (CDA), joint in-phase and quadrature SVA (described in Eqs. 14 and 15), and separate in-phase and quadrature SVA. CDA is a dual apodization technique that uses complex information in the data to improve the sidelobe behavior. It involves transforming data windowed with Hanning (α = 0.5) and rectangular (α = 0) windows. Considering each in-phase and quadrature component independently, a composite result is formed on a point-by-point basis in the following manner:

1. If the windowed components are of the opposite sign, set the composite value to zero.
2. If the windowed components are of the same sign, set the composite value to the number whose absolute value is a minimum.

CDA uses the additional information in the complex components to determine if there is a window between the Hanning weighting and the rectangular weighting that will null the composite value. This procedure allows an entire family of first-order raised cosine windows to be synthesized from the output of two windows.

The generalized raised cosine window will have a sidelobe roll-off proportional to the number of terms in the expansion. For the first-order raised cosine window, this corresponds to a roll-off of f^3. If an additional term is added in the expansion, the roll-off will increase to f^5, but at the expense of added complexity. After constraining the general form of a second-order raised cosine window for continuity at the boundaries, we have

$$w(n) = 1-\alpha\cos(2\pi n/N) + (\alpha-1)\cos(4\pi n/N)\,, \qquad (16)$$

where $0 \le n \le N$. As before, α can be adapted to yield the optimal window at each point in the inverse domain. Iannuzzelli[12] shows that α is given by

$$\alpha=\mathrm{Re}\left\{\frac{2g(m)-[g(m-2)+g(m+2)]}{[g(m-1)+g(m+1)]-[g(m-2)+g(m+2)]}\right\}, \qquad (17)$$

where $0 \le \alpha \le 4/3$. The output can again be defined in terms of a convolution between the transform of Eq. 16 and $g(*)$:

$$f(m) = g(m) - \frac{\alpha}{2}\left[g(m-1) + g(m+1)\right] + \frac{\alpha - 1}{2}\left[g(m-2) + g(m+2)\right]. \tag{18}$$

COHERENT TOMOGRAPHIC ALGORITHMS

Generating accurate ISAR images using tomographic algorithms requires careful implementation. Two potential pitfalls include insufficient interpolation of the range profile (projection) and inaccurate representation of the raw frequency data. Either dramatically hinders image formation.

The back-projection algorithm presented previously did not account for discrete data samples. It assumes that a continuous range profile is available. Since this is not the case, the data must be interpolated in a sufficient amount to minimize errors when projecting onto a discrete image grid. For the images presented in this article, all of the range profiles were oversampled 10 times relative to the grid dimensions. The range profile was interpolated by zero-padding the frequency data prior to inversion. When back-projecting, the nearest point in the profile was selected as the value for the grid point. This method proved to be computationally more efficient than linearly interpolating the range profile during the back-projection process for each individual point.

Coherent back-projection requires the phase of each range profile to be properly represented. Therefore, the raw frequency data must be translated relative to the place in the spectrum where the data were acquired. This translation amounts to a multiplication in the spatial domain with a complex sinusoid that affects only the phase of the range profile. This operation is similar to the focusing correction in conventional ISAR processing. Care must be taken in the application of the phase correction, as it can be aliased during the back-projection process if the range profile was insufficiently interpolated.

With the preceding discussion in mind, two slightly different tomographic algorithms were designed to reconstruct the raw ISAR data. Both algorithms share a common back-projection implementation but differ in the application of the adaptive spectral window. The "radial" algorithm applies the adaptive window directly to the raw data prior to interpolation, whereas the "interpolative" algorithm applies it afterwards. With the radial algorithm, the adaptive window parameter and convolution are calculated only on real data points, making the radial algorithm computationally more efficient. The three-point SVA formulation described by Eq. 15 was used with both the radial and interpolative algorithms, and the five-point formulation described by Eq. 18 was used only in the interpolative algorithm. These algorithms were compared, and results are given in the next section.

Both the radial and the interpolative algorithms rely on the application of an SVA window to each projection prior to back-projecting. Since both algorithms reduce sidelobes in the projection to a degree greater than or equivalent to the reduction of the Hanning window technique, it seems safe to assume that the resulting image will also display the same character. This would certainly be true if the projections were real (as in X-ray tomography); however, this logic breaks down when one considers a complex projection. The complex projection requires a back-projection algorithm to perform complex integrations to form the image. Since the formation is linear, the phase of the projection becomes important. SVA, being a nonlinear technique, affects the phase of each projection. When the image is built using these projections, the sidelobe level is not necessarily lower than that of the Hanning window everywhere, because no constraint was put on the phase at each point in the projection. Experimentally, it has been shown that sidelobe reduction is hindered wherever multiple sidelobes interfere. In one of the results, an apodization was performed on the five-point interpolative window with the Hanning window. A more formal solution has been devised by the author and is currently under investigation.

RESULTS OF ALGORITHM EVALUATIONS

Three data sets were used to evaluate the coherent tomographic algorithms discussed in the previous section. One data set consisted of eight simulated point reflectors arranged in an "aircraft" configuration. These data were used to debug and evaluate the algorithms. The other two data sets contained C-band and X-band RCS data collected on the BQM-74E target drone at RRL. The C-band data are of lower resolution than the X-band data since the measurement bandwidths were 1 and 4 GHz, respectively. For comparison with the radial and interpolative algorithms, coherent tomographic images were also computed using rectangular and Hanning windows. The images resulting from applying these various coherent tomographic algorithms to the three data sets are shown in Figs. 6 to 8.

In all of the data sets, it is apparent that the sidelobes of the rectangular window are contaminating the image (Figs. 6a, 7a, and 8a). The application of a Hanning window to the data prior to back-projection reduces the sidelobes; however, the resolution loss is quite apparent (Figs. 6b, 7b, 8b). In the target drone images, this resolution loss produces blurring in the various images, which is very apparent in the target drone reconstructions.

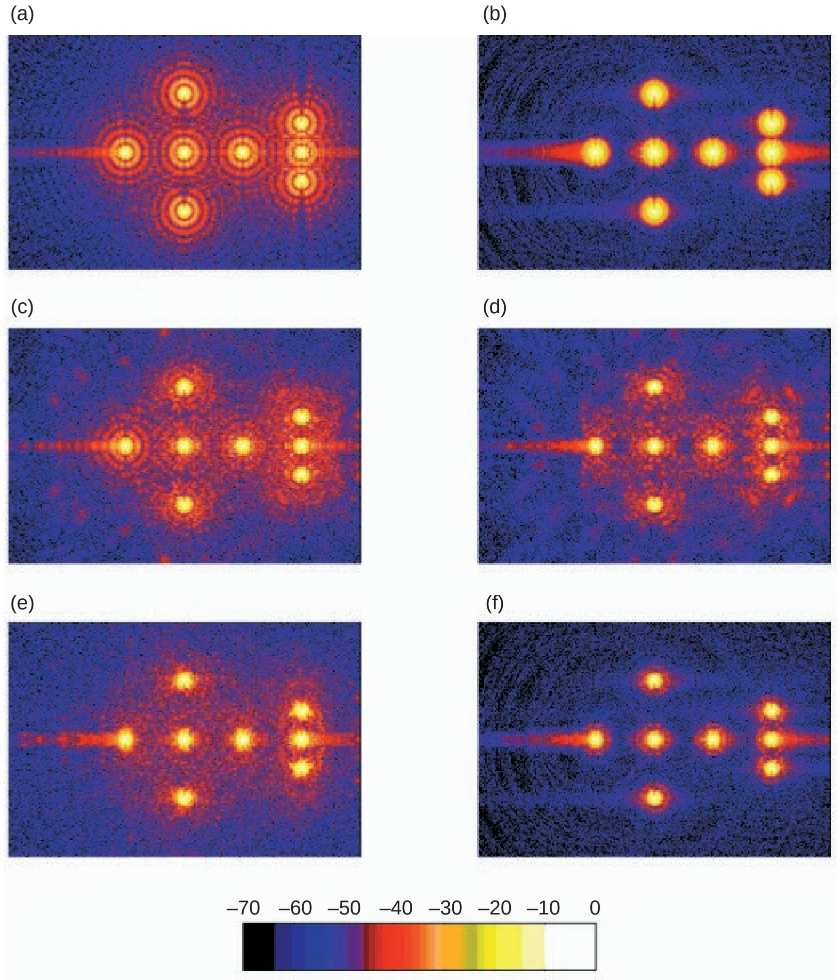

Figure 6. Normalized RCS images formed from point simulation data using coherent back-projection. (a) Rectangular window, (b) Hanning window, (c) radial three-point SVA, (d) interpolative three-point SVA, (e) radial five-point SVA, and (f) interpolative five-point SVA. Each image is scaled to represent a 4 × 6 m area.

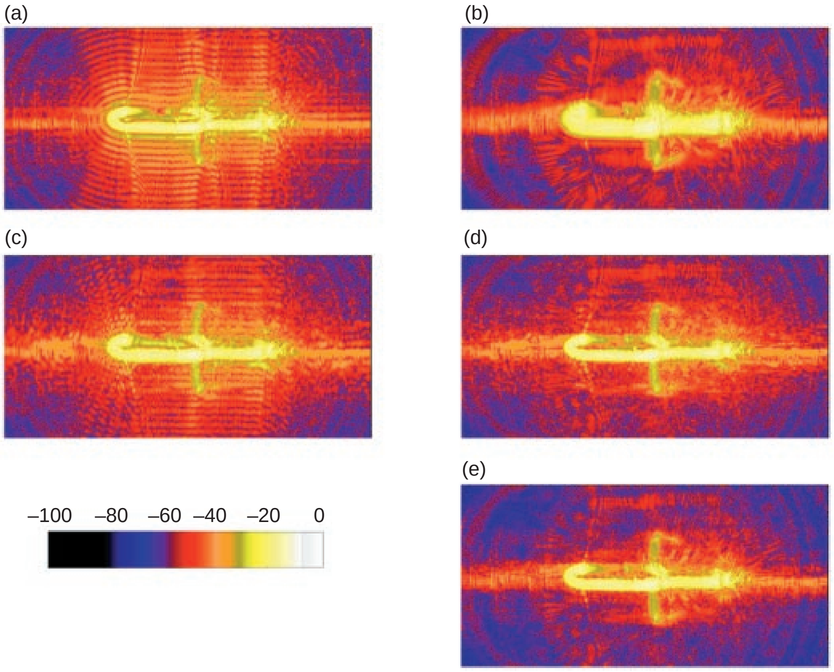

Figure 7. Normalized RCS images formed from 1-GHz C-band BQM-74E RCS data using coherent back-projection. (a) Rectangular window, (b) Hanning Window, (c) radial three-point SVA, (d) interpolative three-point SVA, and (e) interpolative five-point SVA. Each image is scaled to represent a 4 × 8 m area.

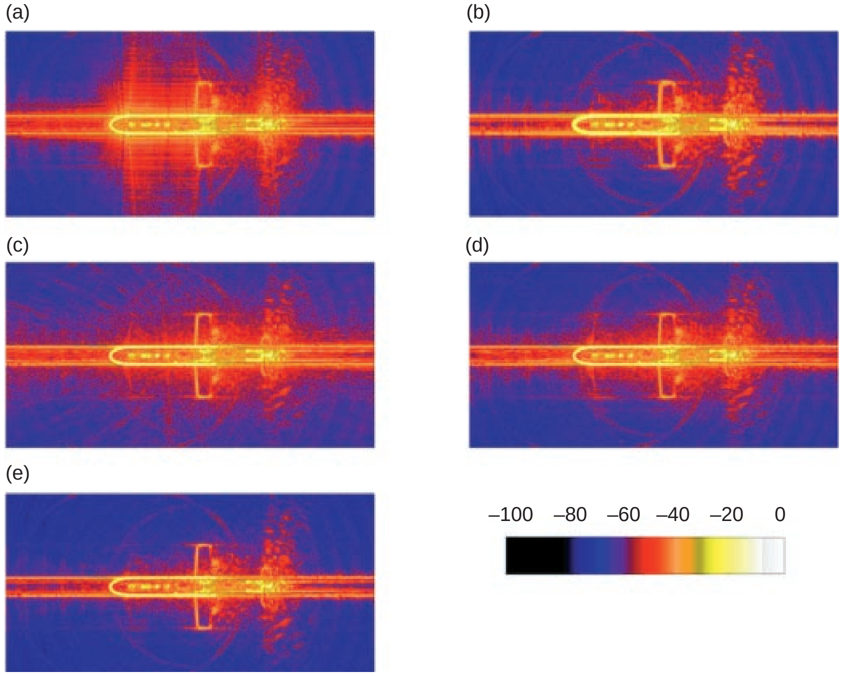

Figure 8. Normalized RCS images formed from 4-GHz X-band BQM-74E RCS data using coherent back-projection. (a) Rectangular window, (b) Hanning Window, (c) interpolative three-point SVA, (d) interpolative five-point SVA, and (e) composite (Hanning and interpolative five-point SVA). Each image is scaled to represent a 4 × 8 m area.

Concentrating on the simulated data set (Fig. 6), we see that the images resulting from the application of the radial and interpolative algorithms constrain the width of the mainlobe of each point source to be equivalent to that of the rectangular window. Thus, the maximum possible resolution is retained. It is apparent, however, that the radial algorithms are limited in their ability to reduce sidelobes in the reconstructed images (Figs. 6c and 6e). When the interpolative algorithms are applied to the process, the sidelobe levels are suppressed to a much greater degree, with the five-point algorithm (Fig. 6f) performing better than the three-point algorithm (Fig. 6d).

Now turning to the BQM-74E target drone RCS data collected at RRL, consider the C-band images generated with a bandwidth of 1 GHz (Fig. 7). Again, heavy sidelobe artifacts are apparent in the reconstruction with the rectangular window (Fig. 7a), and again the application of a Hanning window prior to back-projection decreases resolution in the reconstructed image (Fig. 7b); however, there is good sidelobe rejection. When the radial three-point window is applied to the data (Fig. 7c), the sidelobe reduction is dubious at best. This can be contrasted with the three-point and five-point interpolative algorithms (Figs. 7d and 7e), which provide good sidelobe rejection without trading spatial resolution. In the C-band reconstructions of Fig. 7 it is unclear why the upper half of the drone body shows a significantly smaller RCS than the lower half. This result is not an artifact of the reconstruction process; whether it is a propagation phenomenon or an artifact of the measurement process is unknown.

The RCS imbalance in the C-band reconstructions of Fig. 7 is not evident in the X-band images of Fig. 8. Since the X-band images were acquired at a bandwidth of 4 GHz, the resolution is 4 times greater than that of the C-band images. In these images, sidelobe artifacts are again evident in the rectangular windowed data in Fig. 8a, and the application of a Hanning window shows loss of resolution as seen in Fig. 8b. Applying the three- and five-point interpolative algorithms to these data yields Figs. 8c and 8d, respectively. The five-point formula is particularly well suited to the high-resolution X-band image, where small details are much more apparent. Features that can be seen easily include antennas on the front body of the drone, air intake on the bottom, horizontal and vertical stabilizers, engine nacelle, and parachute dome on the back of the drone. Finally, the composite image shown in Fig. 8e is the result of performing a point-by-point minimization on the Hanning and five-point interpolative images as previously described. This technique provides greater sidelobe reduction; the nonlinear artifacts due to the SVA algorithm are further suppressed.

CONCLUSION

When the relative motion of a coherent wideband radar and a target is such that a circular synthetic aperture can be formed, tomographic processing can be applied to form an image. With this processing, the image can be formed incrementally as the data become available. In discrimination or identification applications, a partial image might be sufficient for a classification; thus, tomographic processing could improve response time in applications where images are used. One particular application might be to image rotating warheads and debris from missile intercepts.

In this article, it was shown that one-dimensional multi-apodization techniques can be applied to the range profiles prior to back-projection to reduce sidelobes in the two-dimensional image. With this application of the one-dimensional windows, dependence in the ordinal directions is removed and each incremental image “shares” in the sidelobe reduction. The five-point formulation of the SVA algorithm was shown to perform best in reducing the sidelobe artifacts in the reconstructed image. Particularly since a native two-dimensional implementation of the five-point formulation has not been devised, this technique offers a potentially powerful tool in image reconstruction.

REFERENCES

[1] Carrara, W. G., Goodman, R. S., and Majewski, R. M., *Spotlight Synthetic Aperture Radar Signal Processing Algorithms*, Artech House, Boston (1995).

[2] Wiley, C. A., "Synthetic Aperture Radars," *IEEE Trans. Aerospace Electron. Sys.* **AES-21**(3), 440–443 (May 1985).

[3] Radar Reflectivity Laboratory Report, *Radar Cross-Section Measurements of the BQM-74E Drone Target for the Mountain Top Project*, Code 4kM500E, Naval Surface Warfare Center, Point Mugu, CA (Sep 1995).

[4] Kak, A. C., *Principles of Computerized Tomographic Imaging*, IEEE Press, New York (1987).

[5] Munson, D. C., Jr., O'Brien, J. D., and Jenkins, W. K., "A Tomographic Formulation of Spotlight-Mode Synthetic Aperture Radar," *Proc. IEEE* **71**(8), 917–926 (Aug 1983).

[6] Mensa, D. L., *High Resolution Radar Cross-Section Imaging*, Artech House, Boston (1991).

[7] Bracewell, R. N., *Two Dimensional Imaging*, Prentice Hall, Englewood Cliffs, NJ (1995).

[8] Bracewell, R. N., *The Fourier Transform and Its Applications*, 2nd Ed., McGraw Hill, New York (1986).

[9] Walker, J. L., "Range-Doppler Imaging of Rotating Objects," *IEEE Trans. Aerospace Electron. Sys.* **AES-16**(1), 23–52 (Jan 1980).

[10] Stankwitz, H. C., Dallaire, R. J., and Fienup, J. R., "Nonlinear Apodization for Sidelobe Control in SAR Imagery," *IEEE Trans. Aerospace Electron. Sys.* **AES-31**(1), 267–279 (Jan 1995).

[11] Nuttall, A. H., "Some Windows with Very Good Sidelobe Behavior," *IEEE Trans. Acoustics, Speech, Signal Process.* **ASSP-29**(1), 84–91 (Feb 1981).

[12] Iannuzzelli, R. J., "Adaptive Windowing of FFT Data for Increased Resolution and Sidelobe Rejection," *Proc. IASTED Int. Conf. Signal Image Process.*, pp. 246–252 (Nov 1996).

ACKNOWLEDGMENTS: I would like to thank the technicians and staff at RRL in Point Mugu, California, responsible for providing the excellent quality RCS data of the BQM-74E target drone, without which accurate reconstructions would not be possible. I also thank Alexander S. Hughes and Russell J. Iannuzzelli for their guidance and help in certain phases of this work.

THE AUTHOR

ALLEN J. BRIC received B.S. and M.S. degrees in electrical engineering from Purdue University in 1989 and 1991, respectively. During graduate studies, he worked as a research assistant at Argonne National Laboratories, gaining experience in computed tomography. He joined APL's Fleet Systems Department in 1992 and is currently a member of the Associate Professional Staff in the Air Defense Systems Department. His research interests include image processing, radar and time series analysis, information theory, nonlinear filtering, and fractals. His e-mail address is Allen.Bric@jhuapl.edu.